

Getting around Antarctica: new high-resolution mappings of the grounded and freely-floating boundaries of the Antarctic ice sheet created for the International Polar Year

R. Bindshadler¹, H. Choi², A. Wichlacz², R. Bingham³, J. Bohlander⁴, K. Brunt⁵, H. Corr⁶, R. Drews⁷, H. Fricker⁸, M. Hall⁹, R. Hindmarsh⁶, J. Kohler¹⁰, L. Padman¹¹, W. Rack¹², G. Rotschky¹⁰, S. Urbini¹³, P. Vornberger², and N. Young¹⁴

¹Code 614.0, NASA Goddard Space Flight Center, Greenbelt, MD 20771, USA

²SAIC, NASA Goddard Space Flight Center, Greenbelt MD 20771, USA

³School of Geosciences, University of Aberdeen, Aberdeen, AB24 3FX, UK

⁴National Snow and Ice Data Center, University of Colorado, Boulder CO 80309-0449, USA

⁵Code 614.1, NASA Goddard Space Flight Center, Greenbelt MD 20771, USA

⁶British Antarctic Survey, High Cross, Madingley Road, Cambridge, CB3 0ET, UK

⁷Alfred Wegener Institut for Polar and Marine Research, Postfach 12 01 61, 27515 Bremerhaven, Germany

⁸Scripps Institute of Oceanography, University of California at San Diego, 9500 Giman Drive, La Jolla CA 92093, USA

⁹Climate Change Institute, University of Maine, Orono ME 04469, USA

¹⁰Norwegian Polar Institute, Polar Environmental Centre, 9296 Tromsø, Norway

¹¹Earth and Space Research (ESR), 3350 SW Cascade Ave., Corvallis, OR 97333-1536, USA

¹²Gateway Antarctica, University of Canterbury, Private Bag, Christchurch 8140, New Zealand

¹³Istituto Nazionale di Geofisica e Vulcanologia, Via di Vigna Murata, 605, 00143 Rome, Italy

¹⁴Australian Antarctic Division, University of Tasmania, Kingston, Tasmania 7050, Australia

Received: 28 December 2010 – Published in The Cryosphere Discuss.: 19 January 2011

Revised: 22 June 2011 – Accepted: 27 June 2011 – Published: 18 July 2011

Abstract. Two ice-dynamic transitions of the Antarctic ice sheet – the boundary of grounded ice features and the freely-floating boundary – are mapped at 15-m resolution by participants of the International Polar Year project ASAIL using customized software combining Landsat-7 imagery and ICESat/GLAS laser altimetry. The grounded ice boundary is 53 610 km long; 74 % abuts to floating ice shelves or outlet glaciers, 19 % is adjacent to open or sea-ice covered ocean, and 7 % of the boundary ice terminates on land. The freely-floating boundary, called here the hydrostatic line, is the most landward position on ice shelves that expresses the full amplitude of oscillating ocean tides. It extends 27 521 km and is discontinuous. Positional (one-sigma) accuracies of the grounded ice boundary vary an order of magnitude ranging from ± 52 m for the land and open-ocean terminating segments to ± 502 m for the outlet glaciers. The hydrostatic

line is less well positioned with errors over 2 km. Elevations along each line are selected from 6 candidate digital elevation models based on their agreement with ICESat elevation values and surface shape inferred from the Landsat imagery. Elevations along the hydrostatic line are converted to ice thicknesses by applying a firm-correction factor and a flotation criterion. BEDMAP-compiled data and other airborne data are compared to the ASAIL elevations and ice thicknesses to arrive at quantitative (one-sigma) uncertainties of surface elevations of ± 3.6 , ± 9.6 , ± 11.4 , ± 30 and ± 100 m for five ASAIL-assigned confidence levels. Over one-half of the surface elevations along the grounded ice boundary and over one-third of the hydrostatic line elevations are ranked in the highest two confidence categories. A comparison between ASAIL-calculated ice shelf thicknesses and BEDMAP-compiled data indicate a thin-ice bias of 41.2 ± 71.3 m for the ASAIL ice thicknesses. The relationship between the seaward offset of the hydrostatic line from the grounded ice boundary only weakly matches a



Correspondence to: R. Bindshadler
(robert.a.bindshadler@nasa.gov)

prediction based on beam theory. The mapped products along with the customized software to generate them and a variety of intermediate products are available from the National Snow and Ice Data Center.

1 Introduction

One of the most basic features of the Antarctic ice sheet is its boundary. However, even utilizing the broad spatial coverage afforded by satellite data, comprehensively mapping the boundary of a region the size of Antarctica is an inherently challenging undertaking. The International Polar Year 2007–2009 (IPY) called for benchmark data sets and provided the motivation for the mapping reported here. The broader goals of that IPY project, called Antarctic Surface Accumulation and Ice Discharge (ASAIID) are yet to be completed, but the ASAIID intermediate products described here have extensive applicability beyond the specific project goals.

The boundary of the grounded ice sheet includes a variety of situations: glacier tongues, where the ice thickness gradually decreases to zero; ice cliffs, where ice breaks off and falls onto the ground or sea ice or into the ocean; and ice shelves, where ice flows into the ocean and remains attached to the grounded ice sheet until it calves, forming icebergs. The last case of flow from grounded ice into floating ice shelves has received considerable attention because it is the dominant situation in Antarctica and represents a significant dynamic shift in the stress state that has challenged ice-flow modelers (see Schoof, 2007 for a recent treatment of the transitional ice dynamics). This case also is complicated by the effects of oscillatory ocean tides that alter the grounded state of ice in the vicinity of the ice sheet boundary and can dramatically alter the speed of the discharging ice sheet (Anandakrishnan et al., 2003; Bindschadler et al., 2003; Wiens et al., 2008). These complexities are worth tackling because it is across this interface that the ocean influences the ice sheet (through the ice shelf) (e.g., Payne et al., 2004, 2007; Joughin et al., 2010) and changes of the interior grounded ice sheet are amplified as they propagate toward this boundary. It is also in this region that the changes in both ice thickness and ice velocity are largest (as expected by ice dynamics theory) (Shepherd et al., 2002; Thomas et al., 2004; Pritchard et al., 2009). The relatively low subglacial bed slopes in these areas (slopes of 10^{-3} to 10^{-5} are typical) amplify relatively small local changes in ice thickness to relatively large horizontal shifts in the boundary between grounded and floating ice, illustrating the value of repeatedly mapping this boundary as a sensitive indicator of change.

In the region where the seaward-flowing ice sheet loses contact with the bed, part of the ice sheet is ephemerally grounded by ocean tides and the connected ice shelf is prevented from fully floating by beam stresses transmitted from the grounded ice. Care is required to ensure that comparisons

between seemingly equivalent data sets do not lead to false conclusions of change. We present new mappings of two important boundaries in this region of the ice sheet: the first is the seaward boundary of surface morphology associated with grounded ice and the second is the landward boundary of freely floating ice shelves. In addition to the positions of these two boundaries, surface elevations of the ice along these boundaries are also extracted from various digital elevation data sets along with a calculation of ice-equivalent ice-shelf thickness (including a correction for lower density firn in the upper layers of the ice shelf). Independent data compiled by BEDMAP (Lythe et al., 2001) are used to quantify the accuracy of the elevations and ice thicknesses assigned to our boundaries. Finally, the separation between the boundaries is examined with a beam flexure theory.

2 The grounding zone

Attempts to define the boundary of the grounded ice sheet and a floating ice shelf have led to the concept of a “grounding line”. However, the term “grounding line” has been applied to available data sets employing different methodologies, some sensitive to different topographic or dynamic features of the region. The use of a single term to refer to different boundaries invites confusion within the science community. The differences in various “grounding lines”, including a careful comparison among a number of “grounding lines”, have been discussed most completely in Fricker et al. (2009).

Far offshore, a floating ice shelf will rise and fall an amount equal to the tidal variations of the ocean in which it floats. However, closer to shore, the stiffness of the ice and the fact that ice well inland is securely resting on the subglacial bed will limit the amount of vertical deflection experienced within the marginal region. The general situation is illustrated in Fig. 1: location F refers to the most seaward point not vertically displaced by tidal flexure even at the highest tide; G is the location where the ice loses contact with the bed (at low tide); I_b and I_m represent inflections of the surface slope where the slope changes most rapidly (the “slope break”) and where the slope is zero (the “hinge line valley”), respectively; and H is the most landward location that experiences vertical motion equal to the magnitude of the tide. Oscillating ocean tides interacting with the floating fringe of the ice sheet will move the point of initial ungrounding landward and seaward as the tide rises and falls.

The boundary in the grounding zone presented in this paper is determined primarily by interpreting the seaward limit of the region of grounded ice features in optical imagery and secondarily from derived surface elevations. Thus, we refer to it as the “ASAIID grounded ice boundary”. It is most consistent with point I_b , the slope break, in Fig. 1. Interferometric analysis of multiple synthetic aperture radar images (InSAR) detects the band of flexure between locations F and H (Fricker et al., 2009); Rignot (1996) refers to the landward

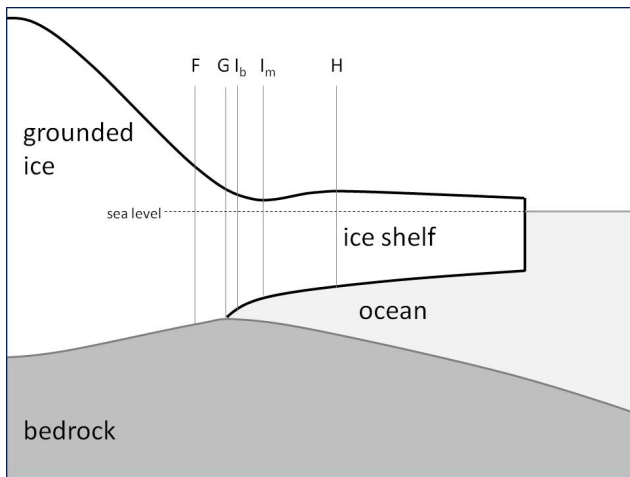


Fig. 1. Schematic of cross-section through the margin of the Antarctic ice sheet. F refers to the most seaward point not vertically displaced by tidal flexure; G is the point where the ice loses contact with the bed (at low tide); I_b and I_m represent inflection points of the surface slope; and H is the most landward point that experiences full tidal flexure (adapted from Fricker et al., 2009). The ASAIID grounded ice boundary is most consistent with point I_b .

limit of this flexure zone as the “hinge line”. Repeat laser altimetry can often detect F and H from repeat-track analysis and I_b and I_m from single profiles (Yamanokuchi et al., 2005; Fricker and Padman, 2006).

Which boundary within the grounding zone is relevant will usually depend on the nature of the science question being posed. The grounded ice boundary we delineate has dynamic significance: the presence of a grounded ice surface morphology demonstrates that not only is the ice contacting the bed, but the ice “feels” the bed sufficiently to react to the stresses associated with this contact resulting in an ice sheet geometry that creates stresses within the ice to accommodate the stresses at the bed. This is distinctly different from identifying an area that becomes grounded briefly during lower tide levels and for which there is no discernable change in the geometry of the ice sheet even though the velocity may be modulated by the tidal oscillations (Anandakrishnan et al., 2003; Bindschadler et al., 2003; Wiens et al., 2008).

Figure 2 illustrates boundaries in the grounding zone from these different approaches for a portion of Antarctic margin near the Ekström Ice Shelf and Neumayer Station. There is broad agreement between the region of flexure zone, defined by the band of dense InSAR fringes, the I_b and H points, defined by the GLAS analysis, and the delineation of the grounded ice boundary, interpreted from the Landsat imagery (discussed in more detail later). However there are some differences, such as in the upper left of the scene where the flexure zone narrows while the hydrostatic line, guided only by the few GLAS points, remains farther offshore. In the inlet near the upper right corner of Fig. 2, the ASAIID

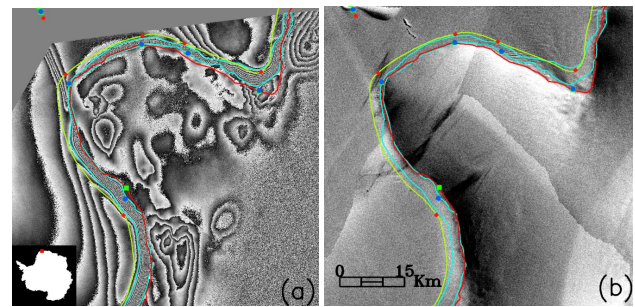


Fig. 2. Section of Antarctic coast (Halvfarryggen Ridge on the Princess Martha Coast with Ekström Ice Shelf on left) 71.6 km \times 69.7 km comparing mappings of different features of the grounding zone with different methods. (a) Interferometric fringe pattern produced by InSAR methods and (b) an enhanced subset of the Landsat Image Mosaic of Antarctica. Cyan lines represent edges of the tidally flexed grounding zone between points F and H (see Fig. 1). Symbols are key points of the grounding zone identified from repeat-track GLAS elevation profiles (F, green square; I_b , blue circle; H, red diamond). Red and green lines are ASAIID grounded ice boundary and hydrostatic lines, respectively.

grounded ice boundary passes farther inland than the band of dense InSAR fringes, but agrees with the I_b point (blue circle) determined from GLAS data. There will always be some differences between boundaries within the grounding zone produced by these different methods, at times due to incorrect interpretation or data quality and availability, but also because different features are being detected. Our observations of the differences between the different boundaries in the grounding zone determined by these various methods, now including the ASAIID grounded ice boundary and hydrostatic line, match those discussed and illustrated at greater length in Fricker et al. (2009).

Previous mappings of the “grounding line” based on satellite optical imagery have been produced and are available through data centers. Two of these familiar to many Antarctic researchers are the “grounding line” contained in the Antarctic Digital Database (ADD) (<http://www.add.scar.org:8080/add/index.jsp>), where the latest revisions were based on prints of Landsat imagery at 1:250 000 scale, and a “grounding line” mapped from the MODIS Mosaic of Antarctica (MOA) at 125-m resolution (Bohlander and Scambos, 2007). A third partial mapping is being released incrementally as coastal change maps (Ferrigno et al., 1996 and <http://pubs.usgs.gov/imap/2600/>). Each of these mapped boundaries corresponds to either the most rapid change in surface slope (e.g., I_b in Fig. 1) or an end of grounded ice (in the case of terminating ice cliffs or grounded glacier tongues). Because each uses a similar visual interpretative method to ASAIID, they are comparable to each other and to the ASAIID grounded ice boundary. Figure 3a illustrates differences between these various boundary products. It appears the data base used in the ADD boundary in this region contained

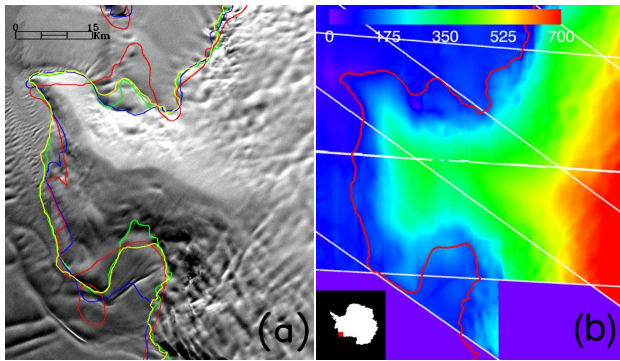


Fig. 3. Section of Antarctic coast (Scott Peninsula along Bakutis Coast) approximately $60 \text{ km} \times 69 \text{ km}$. (a) Enhanced Landsat image comparing various image-based mappings of the “grounding line” or grounded ice boundary: red, Antarctic Digital Database; blue, USGS Coastal Change map series; green, MODIS Mosaic of Antarctica; yellow, ASAD. (b) Color-coded surface elevations (in meters above mean sea level) derived from ASAD application of photoclinoetry using image on left and GLAS elevation profiles. Thin white lines show the location of GLAS profiles interpolated by photoclinoetry. ASAD grounded ice boundary from (a) is reproduced (now in red).

some significant geolocation errors and it is possible some aerial photography may have been included since some portions of this persistently cloudy coast were never adequately imaged with the early Landsat instruments. Reduced spatial or feature acuity might have also contributed to the discrepancies in the ADD boundary. The MOA line is more accurate than the ADD in defining the overall shape of the coastal feature, but at times deviates from the other interpretations when coastal features associated with lightly grounded ice and transitions to the floating ice shelf are encountered. There also are some differences between the USGS coastal change maps and ASAD that we attribute to the fact that the USGS procedure used paper prints of lower resolution Landsat images while ASAD could vary the enhancement of any image in a digital environment to optimize the visual appearance of any local region as different conditions of topography and illumination orientation were encountered along the coast.

3 Data

The primary data sets used to define and provide surface elevations of the grounded ice boundary and hydrostatic line are images from the Enhanced Thematic Mapper Plus (ETM+) instrument onboard the Landsat-7 satellite and surface elevation profiles measured by the Geoscience Laser Altimeter System (GLAS) onboard the Ice, Cloud, and Land Elevation Satellite (ICESat). The Landsat data were used in the construction of the Landsat Image Mosaic of Antarctica, another IPY project (Bindschadler et al., 2008). This image set con-

sists of mostly cloud-free images. They also cluster within a relatively narrow time window (1999–2003). All images were accessed from the USGS EROS Data Center, usually by ftp-download after a visual review of possible candidate images that cover the appropriate region of the ice sheet perimeter. 196 images of this collection cover the entire grounded ice boundary to 82.5° S . Farther south, two ASTER images provide coverage that complete the Ronne Ice Shelf portion of the grounded ice boundary, and imagery from MOA is used to complete the southernmost section of the Ross Ice Shelf. For all but the MOA imagery, the panchromatic band image was visually interpreted at full 15-m resolution (panchromatic band) to identify the grounded ice boundary (cf., Fig. 3a).

GLAS/ICESat data of precise surface elevation information along satellite groundtracks is used in three different ways. The first two uses employ the set of F , I_b and H points available from the National Snow and Ice Data Center (Brunt et al., 2010a). The locations of most rapid slope change I_b , determined along single profiles are used to help confirm the identification of the grounded ice boundary based primarily on the imagery. The H locations, determined by a differencing technique employing repeat GLAS passes collected at different phases of the tide to reveal the tidal flexure of the ice shelf as described in Fricker et al. (2006), are used to determine the position of the hydrostatic line. The third use of the GLAS elevation profile data are in combination with the ETM+ images to produce surface elevation fields through application of photoclinoetry (Wildey, 1975; Bindschadler and Vornberger, 1994).

4 Methods

To satisfy the IPY objectives of international collaboration and inspiring young researchers, the ASAD project invited partners across the world to participate. Customized software was created, along with appropriate documentation describing standardized procedures so that the eventual aggregate product is as uniform as possible. The Antarctic perimeter was divided into a number of segments with different ASAD participants accepting responsibility for mapping portions of the grounded ice boundary and producing photoclinoetric elevation fields for that segment (the hydrostatic line and elevation selection were completed at the end of the project exclusively at NASA Goddard Space Flight Center). The software is designed so that the participant’s results are written to files with standardized names, facilitating both review of the data at NASA Goddard, but also easing the combination of multiple participant results into a single aggregate. Ultimately, all data products were reviewed by the Principal Investigator (Bindschadler, 2010) and final responsibility for their content and quality rests there.

4.1 Grounded ice boundary

Our procedure starts with selecting a particular ETM+ image covering the desired section of the Antarctic perimeter and downloading it from USGS EROS Data Center website. The ASAIL software uses the image metadata supplied with the image to determine the sun azimuth for the image and rotates the image to a sun-at-the-top orientation (required for the later photogrammetry procedures). The software then displays the rotated image on a computer monitor and superimposes the location of ICESat reference groundtracks on the image. Actual groundtracks usually lie within 100 m of the reference groundtracks. Next, to reduce computer memory requirements and file sizes, the user defines sub-images to work on that encompass sections of the expected grounded ice boundary and include ICESat tracks near the top and bottom edges of the sub-image (so a photogrammetric elevation field spanning most of the sub-image can be produced). Once the sub-images are defined, each is written to a separate file directory and the GLAS data for that region are parsed from the complete set of GLAS data (provided to each ASAIL user) and also written to the same directory. The GLAS data used are the GLA06 product (Release 28 and 29) from observation periods 2A (4 October 2003 to 19 November 2003) through 3K (4 to 19 October 2008) (Zwally et al., 2003). Both releases include an ocean tide correction which was retained; however, the saturation correction (`i_satElevCorr`) was only applied to Release 28 data as advised by ICESat data product experts (J. Saba, personal communication, 2009). The processed files provide surface elevation values at ground points spaced roughly 172 m apart along the actual groundtracks.

At this point, the user visually reviews the individual GLAS profiles for each reference track (using customized ASAIL software) and selects the profiles most suitable for photogrammetry. Only one profile for each reference track is permissible. Averaged profiles are not used because individual profiles are often separated by tens and sometimes hundreds of meters and the individual laser footprint locations are not aligned. The coastal region of Antarctica is often cloudy, producing large and/or multiple gaps in the profiles. Our application of photogrammetry requires a GLAS elevation both up-sun and down-sun as starting and ending points for the interpolated. In general, the “best” profiles selected are usually the most continuous profiles because they provide the most complete photogrammetrically derived elevations along the grounding ice boundary.

Photogrammetry is then applied within the sub-image to produce elevation values at all image points between GLAS profiles using interpolations based on the image pixel brightnesses (Willey, 1975; Bindschadler and Vornberger, 1994). The technique has been extensively developed for ice sheets where the existence of a homogenous surface of nearly constant albedo satisfies an important assumption for successful

application of the technique. Image pixel brightness is related to surface slope by

$$DN = A \cos \theta + B \quad (1)$$

where DN is the pixel brightness (in sensor units of digital number); θ is the angle between the solar illumination and the surface normal; coefficient A is the product of the solar irradiance, the surface reflectivity and the factor converting radiance to sensor DN units; and B is a bias due the sensor zero-radiance offset and atmospheric scattering (Bindschadler and Vornberger, 1994). In most ice sheet situations, B is negligible and we also choose to make this assumption. Equation (1) is applied independently for each image segment lying between an up-sun GLAS profile and a down-sun GLAS profile. Interpolation distances are kept as short as possible to minimize interpolation errors. To ensure that the GLAS profiles are continuous at the pixel scale, each profile is linearly interpolated across the standard GLAS point spacing of about 170 m as well across data gaps as large as 450 m. Larger gaps remain unfilled which can lead to longer interpolation segments and can create gaps in the elevation field. For each image segment, Eq. (1) is applied after solving for that segment’s unique value of the scaling coefficient, A , using values of the average slope and image average brightness along that segment. This method ensures that the GLAS elevations along profiles remain unchanged although it can produce slight discontinuities between adjacent image segments when the scaling parameter for adjacent image segments varies significantly. These cross-profile discontinuities are sometimes referred to as “curtains” and are more severe the longer the interpolation segments become. The 8-bit quantization of Landsat DN values also contributes randomly to discontinuities between tracks. Alternative implementations of Eq. (1) were considered, but the GLAS data were deemed to be the best-known elevation information, so these values remain fixed. No attempt was made to smooth the resulting discontinuities because, in general, the calculated elevation fields in constant albedo areas lacked artifacts such as these curtains. Figure 3b shows the photogrammetrically derived elevation field for the image in Fig. 3a as well as the pattern of selected GLAS profiles used as control for that elevation field. The angled boundaries of the elevation field in the lower portion of the figure result from the requirement that there be an up-sun and down-sun GLAS elevation point for every interpolation segment.

While photogrammetry is very successful over much of the ice sheet perimeter, conditions of albedo variation not related to surface slope are encountered in some regions that made portions of the photogrammetric results unusable. These conditions include open (dark) ocean, exposed rock and open crevasses. An alternate elevation field is created from the GLAS elevations by applying a Delaunay triangulation scheme. In this instance, only the GLAS data are used; the image data are ignored entirely. The quality of the result varies by location, dependent primarily on the density

of GLAS profiles, but also on the topographic variation of the region. Other, more sophisticated interpolation methods were examined, but they had the propensity for very large errors over sparsely sampled, undulated topography. Ultimately, our more conservative approach was deemed preferable because it provided an elevation value close to the GLAS values and is reliable in providing a value when no other elevation methods work.

At this stage, with the image providing a nadir view of the sub-image region and the derived elevation field providing a view of the three-dimensional shape of the area, the boundary of the grounded ice features is drawn. Both data sets are linked in separate displayed windows on the computer monitor so that cursor movements can be followed in both windows. To assist the user, the displayed range of either gray-scale (of the image) or color scale (of the elevation field) can be adjusted and the user can zoom the displays to view detail at the 15-m pixel level. Guiding the cursor, the user either draws a continuous line, or clicks discrete points that the computer connects with linear segments, displaying the new grounded ice boundary on the image. The MOA “grounding line” is also displayed and provides useful guidance in areas where the ETM+ radiometric resolution (even with adjustable contrast applied by the user) fails to resolve important subtleties of the surface. In other areas, the increased spatial resolution of ETM+ enables corrections to the MODIS “grounding line” (cf., Fig. 3a).

The primary visual guide to tracing the precise location of the grounded ice boundary over most of the ice sheet perimeter is the visual detection of a change in image brightness that corresponds to the localized slope break between a relatively steep slope on the grounded ice and a relatively shallow slope seaward. The smoother surface of either the floating ice shelf or the fast sea ice relative to the more undulated surface associated with grounded ice features emphasizes this boundary. Marine features, such as offshore icebergs, sea ice lead and floe structures, or open ocean assist in identifying non-grounded regions. However, even with these numerous clues, defining the boundary at the full 15-m resolution is often challenging because the spatial scale of the transition can be many pixels wide. In such regions, the ability to change the image enhancement and zoom to any scale greatly assists precise positioning of the grounded ice boundary. In some regions, the GLAS profiles are useful in precisely locating the point of maximum slope change and the software allows single profiles to be displayed with a linked cursor function that ties position along the profile to the image at the single pixel level.

Bare rock is very easily identified, but uncertainty regarding the possible presence of seasonal snow often requires judgments as to the inclusion or exclusion of individual patches of bare rock within the ice sheet boundary. These situations often have a fractal nature to them and some smoothing is applied by both the operator’s initial drawing and by post-drawing software (described later) to be practi-

cal. Some false extension of the ice sheet is possible due to seasonal snow and future monitoring of the ice sheet boundary in regions prone to this effect should be evaluated carefully.

The most challenging sections of the grounded ice boundary to identify are where fast-moving glaciers discharge into ice shelves. In these cases, the glacier is readily identified by surface undulations and the ice shelf by the absence of similar undulations, but the precise position of the boundary between the two is frequently difficult to locate accurately where the undulations become less dense and less distinct gradually. In general, the grounded ice boundary is drawn immediately seaward of the most downstream undulations and other features that appear to be formed by ice flow over regions of basal resistance and upstream of ice shelf features such as ice rumples or isolated ice rises. In these regions, the 8-bit radiometric resolution of the Landsat imagery often is stretched to its limit and the better 12-bit radiometric resolution of the MODIS sensor enables detection of more subtle surface undulations. For this reason, in many outlet glacier cases, the MOA imagery is examined alongside the Landsat imagery and, when the MOA imagery shows additional grounded ice features, the ASAD grounded ice boundary follows the trace of the MOA “grounding line”.

The typically shallow surface and bed slopes in this type of region are well documented and have led to the recognition of lightly grounded ice plains (Thomas et al., 1988; Alley et al., 1989; Corr et al., 2001). These areas also probably exhibit a wide grounding zone, so large differences between the grounded ice boundary, as we define the seaward limit of grounded ice features in the surface morphology, and the hinge line, as identified in InSAR or altimetry data, are to be expected. Nevertheless, the regions that contain visible surface expressions of grounded ice are regions where the ice feels the bed strongly enough that the shape of the ice adjusts to the basal stresses, whereas the absence of these features indicates the ice does not feel the bed enough to change its shape and, with it, its internal stresses. This makes the grounded ice boundary a metric of the internal ice dynamics and, thus, is an important feature to map and to monitor, even on large fast outlet glaciers, regardless of its relation to the hinge line.

The work described above was completed for each sub-image, each in its own file directory. Combining these individual segments into a single continuous grounded ice boundary around the main ice sheet involves many additional steps. Each sub-image’s grounded ice boundary is visually reviewed and, if necessary, revised, amended or corrected. There were 319 individual boundary segments that were combined. Gaps and overlaps between segments are corrected with additional editing. The two largest gaps occur south of 82.5° S, beyond Landsat coverage. On the Ronne Ice Shelf, three ASTER images are used in an equivalent manner and on the Ross Ice Shelf the MOA image is used, also as a proxy for Landsat imagery. In these areas, ICESat coverage

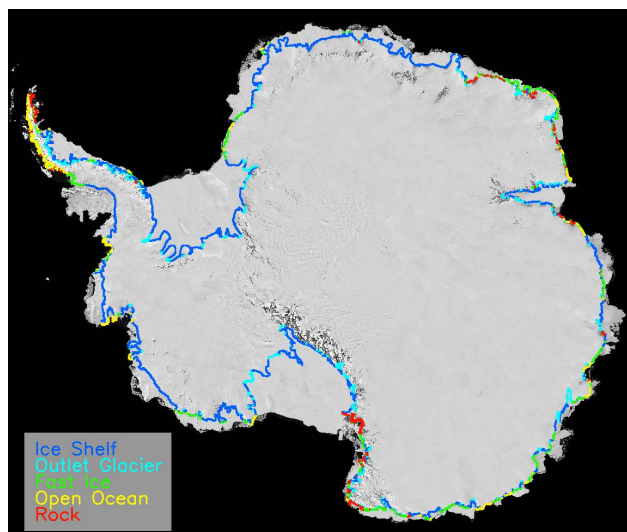


Fig. 4. The ASAID grounded ice boundary displayed on the Landsat Image Mosaic of Antarctica. Line color represents the type of transition for ice transiting the grounded ice boundary. The corresponding percent frequencies of occurrence are: Ice Shelf (dark blue, 61 %); Outlet Glacier (cyan, 13 %); Fast Ice (green, 10 %); Open Ocean (orange, 9 %); and Rock (red, 7 %).

is plentiful, and the photoclinometric elevation fields are high quality, providing an excellent information base from which the grounded ice boundary is drawn. Finally, to remove the unavoidable “jitters” and “stair-steps”, inherent in either a hand-drawn or piecewise-linear line, the drawn lines are smoothed before joining segments. The smoothing approach used a forward-looking algorithm wherein the direction of the redrawn grounded ice boundary is guided by the direction of the next few drawn points rather than only the next point. The details of this approach are provided in separate documentation that will accompany the archived data files (discussed later).

Figure 4 shows the final grounded ice boundary produced by these procedures. It is 53 610 km long and contains 3 574 365 points at a 15-m resolution. The convoluted nature is less apparent at this scale, but for comparison’s sake, the length of the 72° latitude line is 12 350 km. The colors in Fig. 4 indicate the nature of the ice transition at each point along the grounded ice boundary. Each boundary point was determined to be one of five categories: ice shelf; outlet glacier; fast (sea) ice; open ocean; and rock (or land). The number of points and percentage frequencies in each of these transition categories is given in Table 1. The common characteristics defining the outlet glacier class are: a spatially confined flow region, the presence of flow stripes oriented along the expected flow direction, and/or the presence of features on the ice shelf suggestive of a concentrated discharge from the grounded ice sheet. The extent of the outlet glacier was usually taken as the cross-flow “gate” and did not in-

Table 1. Distribution of Antarctic Ice Sheet Grounded Ice Boundary Categories.

Transition Category	# of Points	
Ice Shelf	2 175 363	61 %
Outlet Glacier	478 883	13 %
Fast Ice	361 044	10 %
Open Ocean	325 876	9 %
Rock	233 182	7 %
Total	3 574 348	100 %

clude any margin-parallel segment (that being assigned as an “ice shelf” transition). Differences between the categories of fast ice (which includes possible seasonal sea ice) and open ocean are ephemeral, depending on the specific date of the image used. On-land terminations, where the ice sheet thins to a vanishingly thin wedge adjacent to bare rock, are often highly convoluted and sometimes complicated by seasonal snow cover.

Nearly three-quarters (74 %) of the ice passing the grounded ice boundary transitions to an ice shelf (the combination of the ice shelf and outlet glacier categories). The fast ice and open ocean categories combine to a sub-total of 19 % of the grounded ice boundary, indicating that portion of the ice sheet that flows directly into the ocean and is not connected to an ice shelf fed by the grounded ice sheet. Finally, 7 % of the grounded ice boundary, the vast majority of which occurs in the Dry Valleys region near the northwest corner of the Ross Ice Shelf and the northeastern Antarctic Peninsula, terminates on land above sea level. This relatively high value is associated with the extreme serpentine nature of the grounded ice boundary in these valley incised mountains and includes a few, relatively small, outlet glaciers that terminate on land.

4.2 Hydrostatic line

The hydrostatic line is mapped using the same ASAID software as the grounded ice boundary mapping, but rather than following a brightness feature in satellite imagery, it is drawn such that it is tied to each H point supplied in the F/I_b/H data set derived from repeat-track analysis of GLAS profiles (Brunet et al., 2010a). Between these points, the hydrostatic line is drawn to reflect the general shape of the grounded ice boundary. The smoother shape of the hydrostatic line is intentional, expressing the diffusion of beam supporting stresses onto the ice shelf as has been noticed in interferometric data analyses.

The hydrostatic line can only exist where there is floating ice mechanically connected to the grounded ice sheet, so it is discontinuous around the ice sheet. It occurs predominantly where the grounded ice transitions either to an ice

shelf or to an outlet glacier, but includes a few places where the grounded ice boundary wraps around a coastal nunatak and a continuous ice shelf exists on the seaward side of that nunatak. In some areas, there are no, or widely spaced H points, however, in general, the seaward offset of the hydrostatic line from the grounded ice boundary varies only slowly along the hydrostatic line, increasing our confidence that a reasonably accurate mapping of this feature is possible. An analysis of the seaward offset of the hydrostatic line from the grounded ice boundary appears later. Overall the hydrostatic line contains approximately 1.67×10^6 points for a total distance of 27 521 km, considerably shorter than the grounded ice boundary, reflecting its smoother, discontinuous nature.

While some segments of the ASAIID hydrostatic line are poorly constrained by wide spacings between the H points, there are at least two reasons to attempt its definition. The first is associated with the ultimate goal of ASAIID which is to quantify ice discharge. The H point is defined as the point on an ice shelf closest to land that responds fully to tidal oscillations (Fricker and Padman, 2006). Thus its freeboard is independent of the tidal amplitude and its thickness can be calculated from its surface elevation if the densities of the ice shelf and sea water are known. This enables a means to calculate ice thickness and, when combined with surface velocity (equal to column-averaged velocity on an ice shelf), the discharge can be calculated. This is a valuable set of conditions and even though such discharge calculations will not include basal melting landward of the hydrostatic line, when combined with discharge values at either the hinge line or the grounded ice boundary, they represent another discharge gate and will contribute to quantifying the basal melt between the more-landward gate and the hydrostatic line. A second, more general, reason to map the hydrostatic line is that, just as the grounded ice boundary represents a dynamic boundary separating ice that feels (and does not feel) the bed stresses sufficiently to affect the geometry of the ice, the hydrostatic line represents the boundary beyond which the beam stresses transmitted by the grounded ice sheet through the most-landward portion of the ice shelf are no longer felt. Thus, the hydrostatic line represents another type of dynamic boundary directly related to the transmission of stresses through the ice. As conditions within and around the ice shelf change, the position of the hydrostatic line will change, so mapping and monitoring the hydrostatic line holds the promise of identifying change at the sensitive margins of the Antarctic ice sheet and can be a check on changes inferred from changes in the position of other marginal boundaries (e.g., the hinge line or the grounded ice boundary).

4.3 Positional accuracy

Landsat-7 imagery has a general geo-registration precision of 50 m (one-sigma) (Lee et al., 2004). This precision was confirmed by the misfits experienced with the imagery when the

Landsat Image Mosaic of Antarctica (LIMA) was produced (Bindschadler et al., 2008). Each image was orthorectified, using the RADARSAT Version-2 DEM as part of the LIMA image processing procedure, so this correction is included in the Landsat images used here. Later we establish that in the coastal areas the RADARSAT Version-2 DEM contains errors, as do other DEMs, and while these are generally a few tens of meters, they can exceed 100 m in places. Viewing angles in Landsat imagery are small (less than 10° at the image edge) limiting the impact of orthorectification errors on positional errors, and the elevations along the grounded ice boundary are only a few tens of meters. The end result is that orthorectification-induced positional errors are less than 15 % of the elevation error and can be neglected in most cases.

The error in the identification of the grounded ice boundary on an image varies with the nature of the boundary. When the transition type is either open ocean or rock, the boundary is able to be drawn to the nearest pixel. When a sea-ice transition occurs, the boundary is slightly less obvious, depending on the height difference between the surfaces of the grounded ice and the sea ice and the orientation of the sun relative to the direction of the transition boundary. In general, this boundary can be determined to two pixels (30 m). When the transition consists of slowly flowing grounded ice flowing into a floating ice shelf, the slope break is usually prominent and by zooming in sufficiently to resolve individual pixels, the boundary can be traced to the nearest 3 pixels (45 m). The grounded ice boundary is extremely serpentine. This character limits instances where a slope break is hard to see because it is both straight and oriented in the direction of the solar illumination. The least accurate delineation of the grounded ice boundary is across the mouths of outlet glaciers and ice streams. Here the accuracy varies enormously, based primarily on the spatial density and magnitude of the grounded ice features. As discussed above, the MODIS-based “grounding line” is often relied upon in these instances, but even in that lower resolution image space, the grounded ice features have diffuse edges so we assign a four MODIS pixel error (500 m) error to this boundary. The georegistration and delineation errors are the two major sources of positional error, so overall, our estimates of the positional errors (one-sigma) for the grounded ice boundary are the root-squared-sum of these two contributions: ± 52 m for the open ocean and rock boundaries; ± 58 m for the sea ice boundaries; ± 67 m for the ice shelf boundaries; and a much larger ± 502 m for the outlet glacier boundaries.

The positional accuracy of the hydrostatic line is much poorer. This line is pinned to the H points determined from the repeat ICESat pass analysis and interpolated in between. The positional uncertainty of individual H points from all factors included in their estimation method is stated as ~ 2000 m (Brunet et al., 2010b). Interpolation of the hydrostatic line is only guided by the shape of the nearby grounded ice boundary and likely introduces a few additional

kilometers error. As such, we view the ASAIL hydrostatic line as an initial estimate of the actual position that will be significantly revised once additional repeat pass altimetry or InSAR data of sufficient precision are collected and analyzed.

4.4 Elevations

In the coastal regions of Antarctica, the assumptions required for accurate photogrammetry are violated frequently enough and GLAS elevations are sparse enough that the assignment of elevations to points along either the grounded ice boundary or the hydrostatic line requires the consideration of additional digital elevation models (DEMs). There are a number to choose from, but each has weaknesses in particular regions or is incomplete, so no single elevation data set is sufficient by itself. Thus, our approach considers a number of elevation values in parallel and allows us to select the “best” elevation values based on their adherence to both nearby GLAS data and the shape of the local ice sheet surface inferred from the Landsat imagery and the GLAS data.

The elevation data sets considered include the photogrammetric and triangulation DEMs already discussed. In addition, a DEM based on a combination of radar and laser satellite altimetry (Bamber et al., 2009) and another based primarily on elevations in the Antarctic Digital Database (ADD) in coastal areas and ERS-1 radar altimetry in the ice sheet interior which was used by the RADARSAT project data (Liu et al., 2001) are included. The former, called here the “altimetry” DEM, specifies surface elevations on 1-km postings while the RADARSAT Version-2 DEM provides elevations on 400-m postings. Both are resampled to our 15 m grid using a bi-linear interpolation scheme. Finally, two stereo image-based photogrammetric DEMs are included: the G-DEM based on ASTER stereo imagery (<http://www.ersdac.or.jp/GDEM/E/index.html>) and, in a few available areas, local DEMs based on stereo SPOT imagery provided by the SPIRIT project (another IPY activity) (Korona et al., 2009). All elevation data sets are converted to a common mean sea level reference by using the EGM96 geoid referenced to the WGS-84 ellipsoid.

Additional customized software was developed to accommodate the needs of this elevation-selection task. The work returns to the sub-image level because the photogrammetric and triangulation DEMs exist only for each separate sub-image. For any sub-image, each DEM grid is interpolated to extract that DEM’s elevation values along the trace of the grounded ice boundary. These boundary-following elevation profiles are superimposed on a single display plot (using distinct colors for each DEM) along with single elevation values corresponding to where GLAS elevation profiles cross the grounded ice boundary. Figure 5 shows an example of the computer screen produced by this software. In additional on-screen windows, the photogrammetric, altimetric, RADARSAT and ASTER DEMs are displayed as shaded re-

lief images, rotated and illuminated to simulate the original Landsat sub-image. These shaded relief images are an excellent means to highlight subtle artifacts in each DEM, providing another test of each DEM’s fidelity in matching the surface topography (cf., Fig. 5).

With this visual information, the operator is able to select a portion of the grounded ice boundary, define the best source of elevation data along that segment, and assign a quality (or confidence) rating to those elevations. GLAS data are regarded as “truth”, so elevation values close to the GLAS data are weighted heavily in choosing the preferred elevation source, as well as in rating its quality, but a profile that matches the perceived shape of the surface along the grounded ice boundary is also important. The ability to define the preferred elevation in segments based on the relative, and shifting, strengths of the various elevation sources removes the dependence of the chosen elevations on a single elevation source and is both a critical software feature and an important characteristic of the ASAIL products. Further, the ability to define the beginning and ending of each segment enables the preferred DEM source to switch at crossing points, thus avoiding a discontinuity in the profile of chosen elevations. Not all discontinuities are avoided, however, particularly in the case of small gaps in an otherwise preferred DEM. This was especially true for the SPIRIT DEMs that cover only limited areas and for the ASTER G-DEM that is hampered by the application of an inaccurate coastal mask that omits elevations in regions where it appears that excellent elevations might have been provided in the unmasked, but unfortunately unavailable, DEM. Where discontinuities occur, the quality rating is set to “Poor” (least confident rating) to acknowledge the fact that at least one chosen elevation is incorrect. An additional selectable elevation of “sea level” is available to identify the many instances of the grounded ice boundary occurring with a transition to the open ocean. No DEM correctly captures the elevation discontinuity at these locations. In these cases, the DEMs are ignored and an elevation of zero is specified. This occurs in 9 % of the grounded ice boundary points (cf., Fig. 4 and Table 1).

Figure 6a shows the preferred elevation source for each point along the ASAIL grounded ice boundary; percentage amounts are also given and repeated in Table 2. The photogrammetric DEMs (from ASTER and SPOT) were chosen most frequently; nearly a third (33 %) of all elevations. The photogrammetric technique was particularly well adapted to the rugged topography along the coasts of the Antarctic Peninsula, the Dry Valleys and Victoria Land (the northern portion of the Transantarctic Mountains). The use of photogrammetric elevations probably would have been larger if more DEMs were produced by the SPIRIT project, the ASTER G-DEM data were not poorly masked, or the coverage of either extended south of 82° S. (Note: the unmasked G-DEM data no longer exist but a second version is scheduled for completion in 2011 with the masking issue yet undecided.) Photogrammetric elevations were selected 26 % of

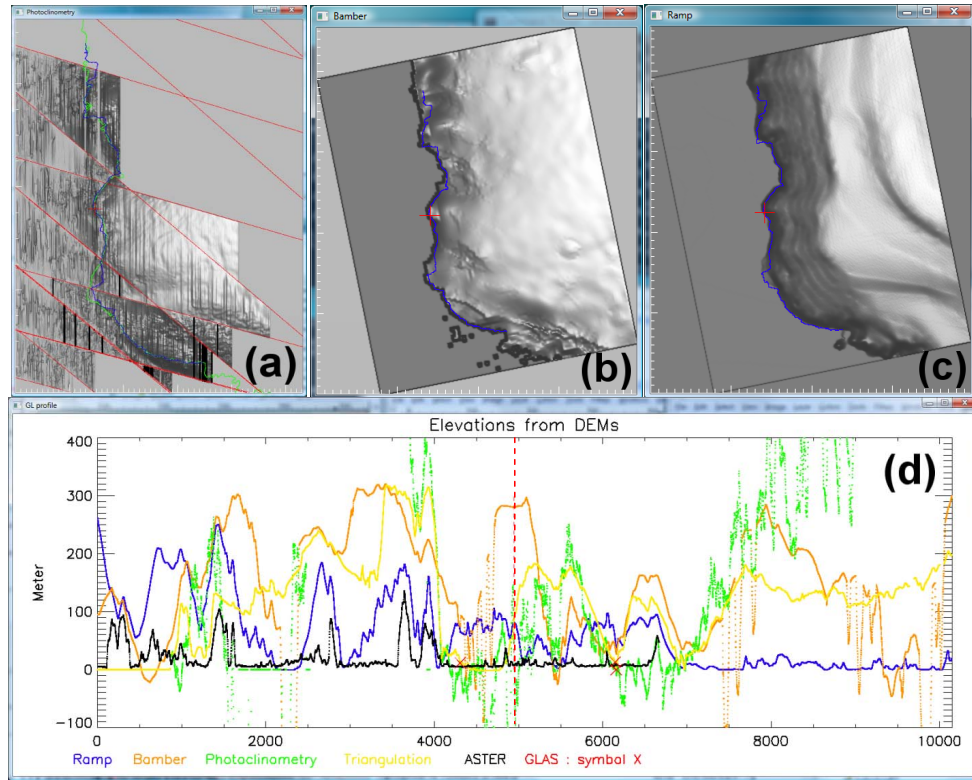


Fig. 5. Sample of screen display for elevation selection operation. (a–c) Shaded relief versions of photoclinometric, altimetric (aka. Bamber, 2009) and Radarsat DEMs, respectively, rotated and illuminated to match the original illumination of the Landsat sub-image. Blue line is the ASAIID grounded ice boundary; green line is the MOA “grounding line”. Red “+” symbols correspond to position of vertical dashed red line in lower panel. (d) Elevation profiles extracted from various DEMs indicated by lines of different color (legend below) with red X’s being ICESat GLAS elevation values positioned where the ICESat profiles crosses the grounded ice boundary. Horizontal axis is in units of 15-m pixels. Vertical axis is elevation in meters above sea level.

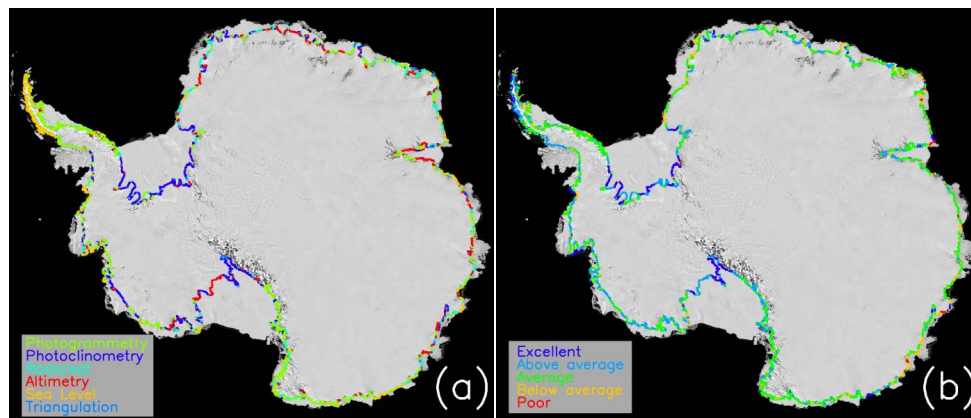


Fig. 6. The ASAIID grounded ice boundary. (a) Colored lines represent the DEM source of selected elevation values. The corresponding percent frequencies of occurrence are: photogrammetry (green, 33 %); photoclinometry (dark blue, 26 %); Radarsat (cyan, 17 %); altimetry (red, 13 %); sea level (orange, 9 %); and triangulation (light blue, 2 %). (b) Colored lines represent the confidence in the selected elevations. The corresponding percent frequencies of occurrence are: Excellent (dark blue, 18 %); Above Average (cyan, 36 %); Average (green, 40 %); Below Average (orange, 5 %); and Poor (red, 0.5 %).

Table 2. Elevation Source for points along grounded ice boundary and hydrostatic line.

Source	Grounded Ice Boundary (%)	Hydrostatic Line (%)
Photogrammetry	33	4
Photoclinometry	26	37
RADARSAT	17	16
Altimetry	13	38
Sea Level	9	0.3
Triangulation	2	5

the time, the next most used elevation source, with the largest region of use being along the grounded ice boundary of the Ronne/Filchner Ice Shelf. RADARSAT and the altimetric DEMs were used 17 % and 13 % of the time, respectively. The triangulation elevations, a worst-case alternative, only needed to be used 2 % of the time.

Table 3 summarizes the frequency of the selected elevations for each confidence class and Fig. 6b shows the spatial distribution. Quantitative accuracies are discussed in the next section. The “Excellent” ranking, reserved for those segments where the elevations matched the GLAS elevations very closely, occurs 18 % of the time and is largely confined to the southernmost boundaries of the Ross and Ronne/Filchner Ice Shelves. “Above Average” confidence (36 % occurrence) is assigned to segments along which there is close agreement with the GLAS elevations and the shape of the profile agrees with a visual interpretation of the imagery (i.e., the simulated image and the actual image were similar). This category also is located most frequently at ice shelf transitions, but is more widespread throughout West Antarctica. Segments ranked with an “Average” confidence in elevations (40 % occurrence) display more variations between DEMs but with a clear preference for the one DEM and are distributed along the entire boundary. “Below Average” confidence (5 % occurrence) usually corresponds to cases where the spread of DEMs is large with none standing out as the obvious choice. In these cases, the preference was usually assigned to the DEM profile that either most closely matches the GLAS elevations or that best expresses the shape of the elevation surface interpreted from the imagery. These are seen to occur in very isolated regions. In the cases of “Poor” confidence (0.5 % occurrence), there were no good elevations to choose from or there are elevation discontinuities along the boundary.

To ensure consistent application of this qualitative confidence assessment throughout the entire data set, the ratings were assigned by a single operator. The spatial pattern of confidence is not obviously correlated with the specific type of boundary – from rugged mountains to very smooth, nearly featureless terrain, to heavily crevassed regions – so its inclu-

Table 3. Elevation Confidence for points along grounded ice boundary and hydrostatic line.

	Grounded Ice Boundary (%)	Hydrostatic Line (%)
Excellent	18	4
Above Average	36	32
Average	40	59
Below Average	5	4
Poor	0.5	0.1

sion in the ASAD product provides an additional indication of elevation accuracy that cannot be gleaned from knowing either the type of transition or the source DEM.

The identical elevation-picking procedure is applied to the hydrostatic line. Figure 7 and Tables 2 and 3 present similar results for the hydrostatic line. The selections and statistics of the preferred elevation sources are distinctly different from those for the grounded ice boundary. In particular, photogrammetry is only selected 4 % of the time and is limited to the rougher coasts. This decrease in use is due to three factors: photogrammetry is most accurate in rugged terrain, where there are sharp features in the stereo imagery, but ice shelves tend to lack these features; there often is no hydrostatic line (i.e., no ice shelf) near some of these areas; and when there is a hydrostatic line, the frequently poor masking of the ASTER G-DEM eliminated potentially useful elevations in these regions. In its stead, at 38 % of the total, altimetry makes a much larger contribution to the chosen hydrostatic line elevations and is distributed across the coast. This is probably due to the smoothing effect of fitting an elevation surface to the altimetric data: a bias toward higher elevations will result at the grounded ice boundary where the slope change is most rapid, but this bias will be much reduced farther out on the ice shelf. Photoclinometry also increases its share of the selected elevations, to 37 %, because it works best in less rugged terrain and uncrevassed regions, but its distribution is still strongly confined to the same regions as for the grounded ice boundary. RADARSAT elevations are used about as frequently for the hydrostatic line (16 %) as for the grounded ice boundary (17 %) but with no particular spatial concentration. Sea level (zero elevation) is chosen less frequently (0.3 %) because the hydrostatic line is not included in open ocean regions.

The qualitative confidence ratings of the hydrostatic line are evaluated in a manner consistent with the grounded ice boundary elevation confidences and by the same operator. Overall, the confidences are lower, with only 4 % in the “Excellent” category; this time nearly exclusively in the southern Ross Ice Shelf and the confidence of much of the Ronne/Filchner Ice Shelf points decreasing to “Above

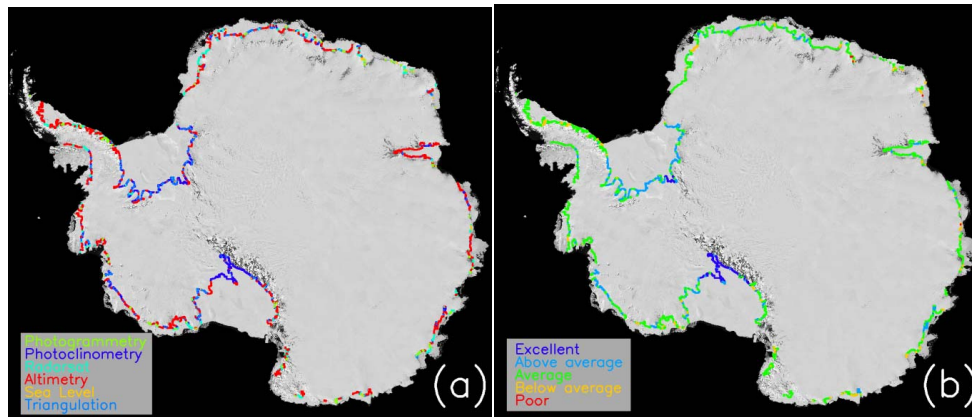


Fig. 7. The ASaid hydrostatic line. **(a)** Colored lines represent the DEM source of selected elevation values. The corresponding percent frequencies of occurrence are: photogrammetry (green, 4 %); photoclinometry (dark blue, 37 %); Radarsat (cyan, 16 %); altimetry (red, 38 %); sea level (orange, 0.3 %); and triangulation (light blue, 5 %). **(b)** Colored lines represent the confidence in the selected elevations. The corresponding percent frequencies of occurrence are: Excellent (dark blue, 4 %); Above Average (cyan, 32 %); Average (green, 59 %); Below Average (orange, 4 %); and Poor (red, 0.1 %).

Average”. “Average” confidence is assigned to the majority (59 %) of hydrostatic line points, covering most of the coast. “Below Average” and “Poor” confidences are assigned to only 4 % and 0.1 % of points, respectively.

4.5 Elevation accuracy

Our elevation selection process includes many elevation sources and demonstrates that none are singularly preferred. To assess the accuracy of our chosen elevations, we compare them to two sets of field data. The first comes from an airborne mission conducted by the British Antarctic Survey (BAS) in the 2006–2007 austral summer, partly to support ASaid validation efforts. Surface elevations and ice thicknesses were measured over approximately 1500 flight kilometers along extensive reaches of the western boundary of the Ronne Ice Shelf from 200 km north of Evans Ice Stream to the north margin of Institute Ice Stream. Because the ASaid mapping of this region had not been completed at the time these data were collected, they do not directly coincide with either the ASaid grounded ice boundary or the hydrostatic line. However, because photoclinometry produces the preferred elevations in this region and this method produces an elevation field at 15-m spatial resolution, a direct comparison of ASaid elevations near the grounded ice boundary and hydrostatic line with BAS measurements at identical locations is possible. The confidence for all the ASaid elevations in this area is divided roughly equally between “Excellent” and “Above Average” (cf. Figs. 6b and 7b). 30 000 points spanning roughly 640 km are used covering the regions of Evans Ice Stream (and northward), across Carlson Inlet and around most of Fletcher Promontory. For each BAS measurement, its location is paired with the calculated elevation of the nearest pixel in the photoclinometry DEM and

shown in Fig. 8. The linear fit through this distribution and forced to pass through (0, 0) has a slope of 0.997 and an R^2 of 0.986. The elevation differences (BAS minus ASaid) produced a Gaussian distribution with a mean difference of 0.24 ± 5.77 m. This region is experiencing a slight thickening of about 0.2 m yr^{-1} (Pritchard et al., 2009). No large elevation difference is expected because the 2006–2007 period of BAS data collection occurs roughly in the middle of the GLAS data time window (late 2003 to late 2008) and the GLAS data are used to control our photoclinometry elevations.

The second comparison of elevations draws upon the BEDMAP compilation of Antarctic field data (Lythe et al., 2001). Although BEDMAP’s primary aim is to produce the best bed elevation map of Antarctica using all available measurements of ice thickness and surface elevation collected over the past 50 yr, some of the missions do include surface elevation data. The extended period represented by the data leave open the question of how much surface elevations may actually have changed from the time of collection to the epoch of our data sets. In addition, the elevation reference surfaces (i.e., geoid and ellipsoid) also have evolved and some of the documents supporting particular BEDMAP missions lack detail on this critical point. Despite these limitations, the BEDMAP data provide an independent and useful set of surface elevations to compare with the ASaid elevations.

The vast majority of the 127 missions compiled by BEDMAP cover interior regions of the ice sheet, but a few contain data that cross the ASaid grounded ice boundary, the hydrostatic line, or both. Crossings are defined as any ASaid point (of either line) that occurs within 30 m of a BEDMAP data point. Other distances were tried, but a shorter distance missed some crossings while a larger

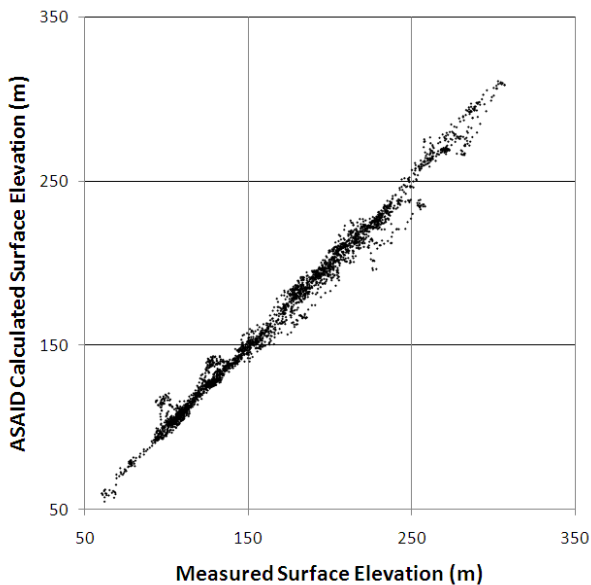


Fig. 8. Surface elevations measured by British Antarctic Survey near grounded ice boundary of Ronne Ice Shelf versus surface elevations at the same locations extracted from a photogrammetry DEM produced by ASAIID.

distance includes too many ASAIID points for a single crossing. 15 missions yield 954 crossing point pairs of the grounded ice boundary and 702 crossing point pairs of the hydrostatic line, clustered on the three largest ice shelves: the Ross, the Ronne/Filchner, and the Amery. Very few additional crossings result from the other missions and because the statistics would not be altered significantly even if they were included, we limit our comparisons presented here to the BEDMAP data in these three areas. These areas are not among the areas experiencing the greatest rates of thickness change (e.g., Pritchard et al., 2009) so the risk of temporal elevation changes compromising our results is reduced.

Because some BEDMAP data sets do not include surface elevations, the number of crossing point pairs for which elevations can be compared is less than the number of crossings. Figure 9 plots the BEDMAP surface elevations against the paired ASAIID surface elevations (including an indication of the chosen DEM source) of the ASAIID grounded ice boundary and Table 4 presents the statistics of both the grounded ice boundary and hydrostatic line comparisons. The data pairs in Fig. 9 are distributed roughly equally on either side of a line of slope 1. The statistical linear fits, forced to intersect the origin (0, 0), considered separately for the 417 pairs of the grounded ice boundary subset and the 262 pairs of the hydrostatic line subset are nearly identical in slope (0.93 and 0.95, respectively) and R^2 (0.64 and 0.66, respectively). There appears to be no strong bias in these comparisons that is related to the selected DEM source with the exception that the Radarsat DEM seems to be biased slightly lower than the BEDMAP elevations.

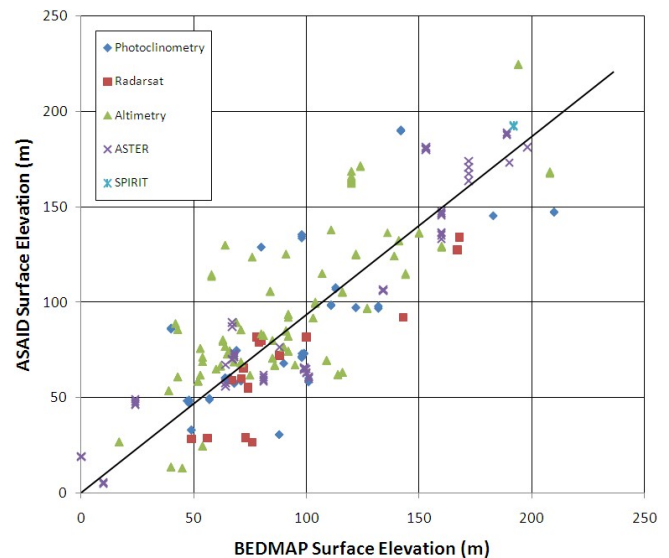


Fig. 9. Surface elevations at common locations along the ASAIID grounded ice boundary extracted from BEDMAP missions versus preferred surface elevations selected from various DEMs by ASAIID. Data symbols identify the source DEM used by ASAIID. Sloped line is a linear fit through all points constrained to pass through (0, 0) (cf. Table 4).

Table 4 also includes measures of the bias and standard deviations of the differences between paired ASAIID and BEDMAP elevations. For the full set of elevation pairs of either the grounded ice boundary or hydrostatic line, the elevation bias is quite small (-4.7 and 1.5 m, respectively) and the standard deviations are also of similar magnitude (26.4 and 21.5 m, respectively). These values are worse than the comparison with the BAS data presented earlier and may reflect some of the limitations (i.e., variable accuracy of BEDMAP elevations, date of collection and reference surface uncertainty) of using the BEDMAP data for this accuracy assessment. Subdividing the BEDMAP-comparison data sets by confidence category (i.e., “Excellent” to “Below Average”) produces bias values that range from -20.8 to 8.1 and standard deviations that range from 13.4 to 28.9. There does not appear to be any correspondence that associates a lower confidence in the elevation value selection with either a higher bias or a higher standard deviation, although some of the data sets are small, particularly for the “Below Average” category and no pairs were found for elevations with “Poor” confidence. The lack of a relation between confidence and accuracy is surprising given the often wide range of DEMs from which elevations were chosen. Because the next section (on ice thickness) also contains quantitative comparisons with BEDMAP data that infer a better accuracy for ASAIID-selected surface elevations, the more complete discussion of elevation accuracy is deferred to the Summary.

Table 4. Comparison of BEDMAP and ASAIID Surface Elevations. Slope and R^2 values refer to linear fits forced to pass through (0, 0) (cf., Fig. 9).

	Number of paired points	Slope of Linear Fit	R^2	Elevation Difference (m) (BEDMAP-ASAIID)
Grounded Ice Boundary				
All Classes	417	0.93	0.64	-4.7 ± 26.4
Excellent only	58	0.75	0.81	-20.8 ± 19.7
Above Average only	92	0.95	0.57	-3.6 ± 28.9
Average only	261	0.94	0.66	-2.7 ± 24.9
Hydrostatic Line				
All Classes	262	0.95	0.66	1.5 ± 21.5
Excellent only	0			
Above Average only	89	0.91	0.67	5.4 ± 23.0
Average only	163	0.98	0.65	-1.0 ± 20.7
Below Average only	10			8.1 ± 13.4

4.6 Ice thickness

Surface elevations on floating ice are sometimes converted to ice thicknesses by invoking the hydrostatic equilibrium condition. While this conversion is sometimes applied immediately adjacent to the grounding ice sheet (e.g., Rignot et al., 2008), it is strictly only valid at the hydrostatic line, seaward of the hydrostatic line, and possibly at one or more locations between F and I_m (see Rignot et al., 2011, Fig. 1 for this final point). The conversion relationship can be written as

$$H_e = \frac{(Z_s - \Delta h)\rho_w}{\rho_w - \rho_i}; \quad \Delta h = h_f \left(1 - \frac{\rho_f}{\rho_i}\right) \quad (2)$$

where H_e is the equivalent ice thickness; Z_s is the surface elevation above mean sea level, h_f and ρ_f are the depth and density of the firn, respectively; and ρ_i and ρ_w are the densities of pure ice and of seawater: 917 and 1026 kg m⁻³, respectively. The term Δh is commonly referred to as the “firn-depth correction” and accounts for the air contained in the surface snow. A detailed meteorological model quantifying this air-in-firn effect has been published by van den Broeke et al. (2008). We were provided a file specifying the correction term on a 0.1 degree grid over the Antarctic continent that we bi-linearly interpolate to the location of each point along the grounded ice boundary and hydrostatic line. The distribution of this firn correction term around the perimeter of Antarctic was confirmed to be equivalent to Fig. 4 in van den Broeke et al. (2008).

In applying Eq. (2), there are a few instances where the firn-depth correction exceeds our surface elevation leading to negative equivalent ice thicknesses. This is clearly incorrect. Such occurrences are distributed widely around the continent and are often associated with where our hydrostatic line extends across short patches of fast ice between longer sections

of floating ice shelf. The single largest concentration of very low elevations occurs between longitudes 40° E and 57° E. To avoid negative thicknesses, a variable coefficient is added to Eq. (2) modifying it to

$$H_e = \frac{(Z_s - f\Delta h)\rho_w}{\rho_w - \rho_i}; \quad f = 1 - e^{-\frac{Z_s}{\Delta h}} \quad (3)$$

The coefficient, f , is only significant when the firn correction depth becomes a significant fraction of the surface elevation. f ranges from unity for large surface elevations to zero when the firn-depth correction is much larger than the surface elevation. Physically this coefficient can be interpreted as reducing the effect of included air in firn when the surface elevation is so low that much of that firn would be flooded by seawater and, presumably refrozen, thus increasing the density and reducing the air content.

Figure 10a shows the distribution of calculated hydrostatic line ice thicknesses around the continent along with a histogram of values. Very thick ice (sometimes over 2000 m) occurs where deep ice streams and glaciers feed the Ross, Ronne/Filchner and Amery ice shelves. The histogram of ice thicknesses (Fig. 10b) approximates a log-normal distribution with the most frequent ice thicknesses in the range 300–400 m. There are two other features to note. The first is the local minimum/local maximum couplet at 800–900 m thickness. We offer no explanation for this feature nor do we associate any significant characteristic of hydrostatic line ice thickness to it. The second feature is the high frequency of occurrence at very small ice thicknesses; 6% of the equivalent ice thicknesses are less than one meter. This might be a real feature, reflecting the frequent occurrence of thin ice, but it also is caused, to some undetermined degree, by errors in measurement of thin coastal ice and the accuracy of geoid knowledge along the Antarctic coast.

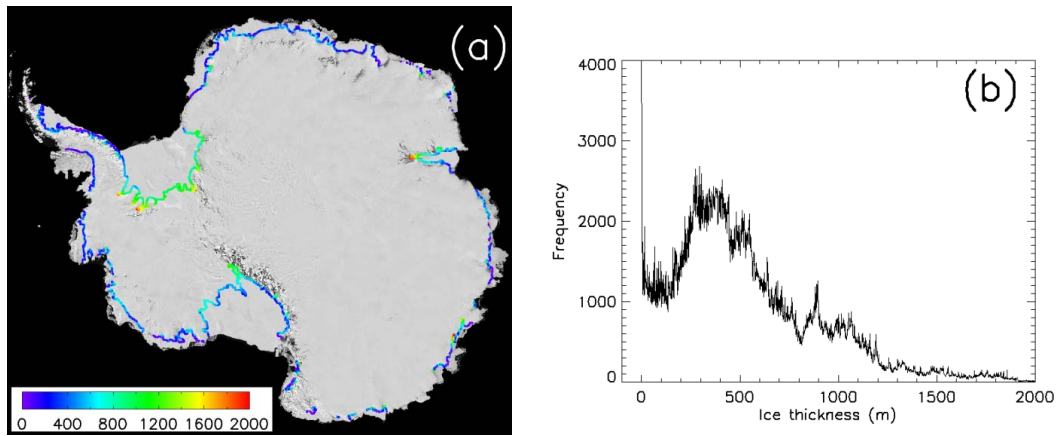


Fig. 10. Ice thickness calculated along the ASAID hydrostatic line (a) mapped on the Landsat Image Mosaic of Antarctica with color representing ice-equivalent thickness in meters (cf., Eq. 3 in text) and (b) presented as a histogram of values.

4.7 Ice thickness accuracy

Our quantitative assessment of ice thickness accuracy uses the same BEDMAP data set employed earlier to assess elevation accuracy. However, unlike those elevation comparisons, ice thickness comparisons are not encumbered by the uncertainty of using a consistent reference surface. There also are more data pairs to compare, because all BEDMAP data sets include ice thickness. The same criterion of pairing each BEDMAP point to any ASAID point within 30 m is applied and, repeating the results, there are 954 crossing point pairs of the grounded ice boundary and 702 crossing point pairs of the hydrostatic line, clustered on the three largest ice shelves: the Ross, the Ronne, the Filchner, and the Amery.

To permit a valid comparison, the ASAID ice thicknesses are first converted from an ice-equivalent thickness to an expected actual ice thickness by accounting for the firn-depth correction included in Eqs. (2) and (3). This is simply done by calculating the expected actual ice-shelf thickness, H_a as

$$H_a = Z_s + H_e \left(\frac{\rho_i}{\rho_w} \right) \quad (4)$$

Figure 11 plots the measured BEDMAP ice-shelf thickness values against the calculated ASAID values of actual ice-shelf thickness (H_a from Eq. 4) for the crossing pairs along the hydrostatic line and Table 5 presents the statistical results. The agreement is considerably better than for the surface elevation comparison (cf. Fig. 9 and Table 4). The linear fit (again forced to intersect the origin (0, 0)) has a slope of 0.94 and an R^2 value of 0.92 with similar results when each of the three areas is considered separately: slopes ranging from 0.90 to 0.97 and R^2 ranging from 0.89 to 0.98 (cf., Table 5). The distributions of ice thickness differences indicate a consistent bias of ASAID calculated ice thickness lower than the BEDMAP-compiled ice thicknesses, although the magnitude of this bias, 41.2 m for all points, varies with the

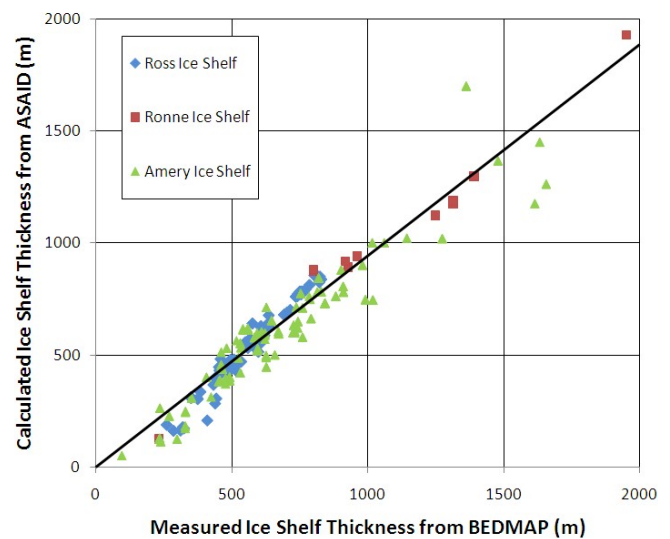


Fig. 11. Ice shelf thickness at common points along the ASAID hydrostatic line extracted from BEDMAP mission measurements versus actual ice thickness calculated from ASAID preferred surface elevations (as described in the text). Data symbols distinguish the three ice shelf regions. Sloped line is a linear fit through all points constrained to pass through (0, 0) (cf. Table 5).

area considered and it is less than one-sigma from zero. It is difficult to identify the source of these differences: real thickness change between the collection times of the data sets, location errors, errors in the ASAID elevation and firn-depth correction errors could all be factors. The Ross Ice Shelf area exhibits the best agreement: 23.6 ± 44.2 m and is the data set collected with the least time difference between data sets.

Subdividing this distribution of thickness differences by confidence level reveals an increased standard error of ice thickness with decreased confidence level as well as a decrease in the fitted R^2 values as ASAID elevation confidence

Table 5. Comparison of BEDMAP and ASAIID Actual Ice Thicknesses. Slope and R^2 values refer to linear fits forced to pass through (0, 0) (cf., Figs. 11 and 12). BEDMAP mission numbers refer to the specific source data sets.

	Number of paired points	BEDMAP Missions	Slope of Linear Fit	R^2	Ice thickness Difference (m) (BEDMAP-ASAIID)
Grounded Ice Boundary					
All points	954		1.03	0.23	-57.3 ± 12.1
Ross Ice Shelf only	508	42, 53	0.99	0.86	9.1 ± 53.5
Ronne Ice Shelf only	25	34, 35, 37, 44, 74	0.95	0.91	86 ± 120.9
Amery Ice Shelf only	417	7–9 and 68–73	1.09	0.05	-139 ± 380
Hydrostatic Line					
All points	702		0.94	0.92	41.2 ± 71.3
Ross Ice Shelf only	231	42, 53	0.90	0.89	23.6 ± 44.2
Ronne Ice Shelf only	26	35, 36, 37, 38, 44	0.96	0.98	56.8 ± 62.9
Amery Ice Shelf only	445	5, 6, 9 and 69–74	0.97	0.92	73.5 ± 98.1
Excellent only	341		1.19	0.98	14.3 ± 29.6
Above Average only	162		0.91	0.93	68.7 ± 79.9
Average only	190		0.91	0.91	66.6 ± 94.7

decreases (cf., Table 5). These trends support our intention of providing users of these data sets a useful guide to indicate the variable accuracy of the elevations (and ice thicknesses derived from them). Applying Eqs. (2) and (4) to these ice thickness accuracies in Table 5, equivalent uncertainties in surface elevation can be extracted. The values are: ± 3.6 , ± 9.6 and ± 11.4 for Excellent, Above Average and Average confidence levels, respectively. Without sufficient data pairs, the uncertainties for confidence levels 4 and 5 remain undetermined by this procedure, but we estimate them to be ± 30 and ± 100 m based on the conditions used to assign them (i.e., the spread among various DEMs and the occasional occurrence of discontinuities).

It has been stated repeatedly that hydrostatic equilibrium does not apply landward of the hydrostatic line. For this reason and to inhibit misuse of the grounded ice boundary data set, the ASAIID data sets do not calculate an ice thickness from the preferred surface elevation along this boundary (although the firn-depth correction is provided for those who wish to take this risky step). However, to examine the magnitude of errors that would be made by assuming hydrostatic equilibrium at the grounded ice boundary, here we convert our ASAIID surface elevations to hydrostatically equilibrated ice thicknesses at the grounded ice boundary points close to BEDMAP points and compare them to BEDMAP values. The procedure to convert the surface elevations to actual ice thicknesses is identical to the procedure described above for the hydrostatic line points. The point pairs are plotted in Fig. 12 and statistics summarized in Table 5 but, in this case, the points are subdivided by region. Grounded ice is expected to have surface elevations higher than if it were floating in hydrostatic equilibrium, so a bias of thicker-than-

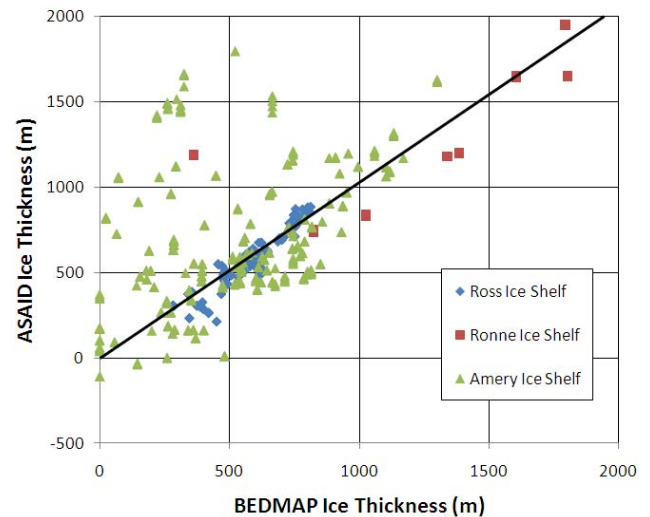


Fig. 12. Actual measured ice thickness at common points along the ASAIID grounded ice boundary extracted from BEDMAP mission data versus actual ice thickness calculated from ASAIID preferred surface elevations. Data symbols distinguish the three ice shelf regions. Sloped line is a linear fit through all points constrained to pass through (0, 0) (cf. Table 5).

measured ice for the ASAIID points is expected. Overall, this bias is apparent in Fig. 12, but when the comparisons are examined separately for the three ice shelves, the agreement on the Ross Ice Shelf is comparable to that for the hydrostatic line, the agreement on the Ronne Ice Shelf is somewhat equivocal and not well sampled, while it is the Amery Ice Shelf points that produce the expected too-thick ice bias. A possible explanation for the favorable agreement for the Ross

Ice Shelf points is that the BEDMAP data were collected in an area of very fast moving, low slope ice streams that include a very extensive ice plain region of lightly grounded ice (Alley et al., 1989). It is in just such a region that the ice is already close to hydrostatic equilibrium even before the ice loses contact with the bed. The large differences found on the Amery Ice Shelf may represent a more typical situation of shorter or nonexistent ice plains where the transition to floating is more rapid; it is in those conditions that extreme caution is advised to avoid significant overestimates in grounding zone ice thickness.

4.8 Application to flexing beam theory

In drawing the hydrostatic line, it was noticed that the seaward offset of the GLAS-determined H points from the grounded ice boundary is relatively consistent locally, but varies gradually from region to region. This characteristic gives us confidence that interpolating the hydrostatic line between GLAS-determined H points is reasonable. Here we use our data set to more quantitatively examine this relationship.

From a purely mechanical point of view, the seaward offset of the hydrostatic line from the grounded ice boundary should depend on the stiffness of the ice, its weight and its thickness. A useful analysis of elastic beam deformation, presented in Vaughan (1995), expresses the beam deflection as

$$w(x) = A_0[1 - e^{-\beta x}(\cos \beta x + \sin \beta x)] \quad (5)$$

$$\beta^4 = 3\rho_w g \frac{1 - \mu^2}{Eh^3} \quad (6)$$

where w is the vertical deflection from mean sea level, A_0 is the full tidal range, ρ_w is the density of seawater, g is gravitational acceleration, μ and E are Poisson's ratio and Young's modulus of ice, respectively, and h is the ice thickness. By examining multiple field data sets, Vaughan (1995) cites a best value of $\beta = 2.43 \pm 0.43 \times 10^{-4} \text{ m}^{-1}$. For our purposes, we require a relationship between ice thickness and the seaward offset of the hydrostatic line from the grounded ice boundary, x_H . For the Rutford Ice Stream examined in Vaughan (1995), x_H is approximately equal to 7000 m, thus $\beta x = 1.7 \pm 0.3$. By substituting this value into Eq. (5) to eliminate β , the following equation relates x_H to ice thickness, h ,

$$x_H = 1.7 \left[3\rho_w g \frac{(1 - \mu^2)}{E} \right]^{\frac{1}{4}} h^{\frac{3}{4}} \quad (7)$$

Using standard values for ρ_w and g , and again referring to Vaughan (1995) for values of μ and E (0.3 and $0.88 \pm 0.35 \text{ GPa}$, respectively) we arrive at the relationship,

$$x_H = (22.2 \pm 6.2)h^{\frac{3}{4}} \quad (8)$$

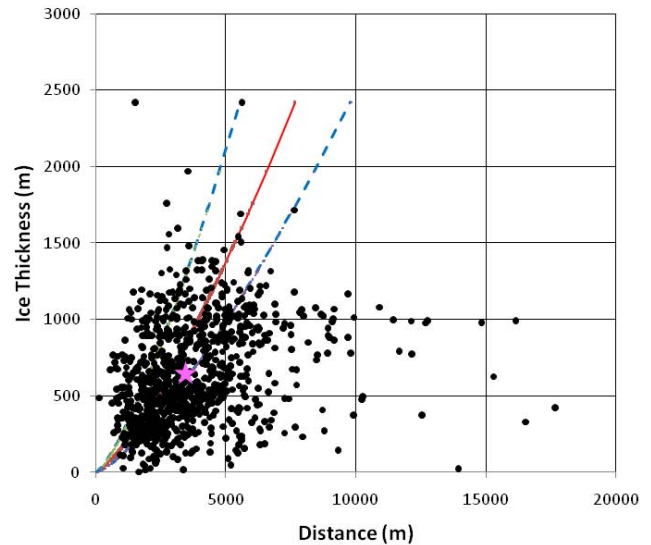


Fig. 13. Relationship of distance between ASAID grounded ice boundary and ASAID hydrostatic line to ice-equivalent thickness. Red line is theoretical relationship (Eq. 7) discussed in the text with blue dashed lines being one standard deviation from this theoretical relationship. Magenta star indicates the position occupied by the mean distance and mean ice thickness of all 930 points.

This relationship is slightly non-linear. The only spatially variables in the coefficient are E and μ , terms that vary with ice temperature, but their effects are diminished through the exponent that appears outside the square bracket of Eq. (7).

Figure 13 presents the distribution of ice thicknesses versus seaward offsets of the hydrostatic line from the grounded ice boundary for the ASAID data sets. The points plotted are selected as being those closest to the 930 GLAS-determined H points so the interpolation between H points does not affect these results. There is considerable scatter, but the first order relationship of increasing offset distance with ice thickness is borne out and the pattern generally matches the relationship suggested by Eq. (8). Both the varying temperature effect and the firm correction effect contribute to the scatter as does the two-kilometer positional uncertainty of the H points (Brunt et al., 2010b). The mean offset distance is $3.7 \pm 2.2 \text{ km}$ and the mean ice thickness is $632 \pm 337 \text{ m}$. The locations of thickest ice occur on the Ronne Ice Shelf near Rutford Ice Stream and on the Ross Ice Shelf near Whillans and Mercer Ice Streams. The locations of largest offsets are scattered around the continent without significant clusters. These results agree reasonably well with the grounding zone width values (Ross: $3.2 \pm 2.6 \text{ km}$ and Ronne: $5.2 \pm 2.7 \text{ km}$) by Brunt et al. (2010b) although it is important to note that their grounding zone width is the longer distance from point F to H, rather than our distance from I_b to H. At best, we can say that our data are consistent with Eq. (8), but it is not possible to use this empirical relationship as a means to define the hydrostatic line from only information on grounded ice boundary position and surface elevation.

5 Distribution and archiving

Ensuring the availability of our ASAIID products in a useful form to the research community is an important objective of this IPY project. The files of the grounded ice boundary and hydrostatic line are generated in such a way to facilitate their use by researchers and have been delivered to the National Snow and Ice Data Center (NSIDC). The latitude/longitude coordinates of each point are given along with our preferred surface elevation and its confidence. Also included are the firn-depth correction, the full set of other surface elevations for each point and point coordinates linked to the specific sub-image used to generate that segment of each line. Finally, the grounded ice boundary file includes the nature of the grounded ice boundary transition (outlet glacier, ice shelf, rock, fast ice or open ocean) and, for the hydrostatic line file, the converted ice thickness (using Eq. (3) and the preferred elevation and interpolated firn correction) is included. Although the grounded ice boundary file does include a surface elevation and the interpolated firn-depth correction term, it does not include an ice thickness value calculated from these parameters because we do not wish to encourage use of an ice thickness value that may be seriously in error (cf. Fig. 12 and the earlier discussion of it).

In addition to the basic grounded ice boundary and hydrostatic line files, we have provided to NSIDC the generating files including the sub-images, line segments, GLAS elevation profiles and derived photogrammetric and triangulation DEMs. It is possible that these files may prove of value either to subsequent research into the data used to produce the higher-order products or to future projects that aim to repeat some or all of what this project accomplished.

Finally, the customized software tools written for ASAIID also have been provided to NSIDC along with detailed documentation as a NASA Technical Memorandum (Bindshadler et al., 2011); however software support will not be supplied. The code is written exclusively in IDL so that anyone can run the various modules using a free-ware IDL engine.

6 Summary and lessons learned

The production of the grounding ice boundary and hydrostatic line at 15-m resolution completes what once seemed a daunting task. The definition of these Antarctic boundaries with the precision achieved by ASAIID offers the research community a valuable new benchmark against which changes can be more conveniently and accurately monitored and quantified. These boundaries are dynamic both in the sense that they shift in time and in the sense that they represent boundaries across which the nature of the ice sheet's interaction with its environment changes. The ASAIID grounded ice boundary represents a significant refinement in a series of "grounding lines" mapped with sim-

ilar data sources, i.e., optical imagery or photography. In contrast, the ASAIID hydrostatic line is new and represents the initiation of what will be progressively improved. By assessing the nature of the transition across the grounded ice boundary, the perimeter of the Antarctic is shown to consist of a floating fringe of ice over 74 % of its length. The main ice sheet terminates on land over only 7 % of the perimeter, the remaining 19 % being a boundary adjacent to either open ocean or sea ice in the ocean.

The inclusion of the surface elevation provides additional utility of these data sets. Our approach of selecting the best elevations highlighted significant inconsistencies within and between various DEMs in the coastal regions of Antarctica. No single DEM can be uniquely preferred. By using precise GLAS laser altimetric elevations, we cull from various DEM sources a higher value composite elevation set along both the grounded ice boundary and hydrostatic line and add our own confidence rating to inform users of the elevation quality on a point-by-point basis.

The assessments of our elevations' accuracy produces mixed results. Comparison with the BEDMAP-compiled surface elevations produces a consistent one-sigma standard error of surface elevation in the low-20 m (cf., Fig. 9 and Table 4), but the BEDMAP elevations contain various errors themselves, some of which are undocumented. Much smaller errors (0.24 ± 5.77 m, cf., Fig. 8) are indicated when elevations from the photogrammetry DEM spanning the ASAIID grounded ice boundary are compared with a nearly contemporaneous and well-controlled data set. The confidences of these elevations are rated as Excellent and Above Average. Similar accuracies are inferred from the ice thickness comparison (cf., Fig. 11 and Table 5). Because these latter results are supported by the expected association of increased errors with decreased confidence in the selected ASAIID elevations, we recommend their use. The recommended, one-sigma elevation uncertainties are: ± 3.6 , ± 9.6 and ± 11.4 m for "Excellent", "Above Average" and "Average" confidence levels, respectively and ± 30 and ± 100 m for the "Below Average" and "Poor" confidence levels.

Computed values of firn densities around the coast enable the conversion of surface elevations to floating ice thicknesses (both ice-equivalent and actual). These compare favorably with measured ice thicknesses (cf., Table 5) despite some large temporal gaps and a bias that indicates ASAIID ice thicknesses are too low by a few tens of meters, depending on location. This comparison also shows the closest correspondence between the confidence assigned to the ASAIID-preferred elevations and the match between the calculated ice thickness and nearby measured ice thicknesses. Our comparison of measured ice thickness against the ice thickness calculated assuming hydrostatic equilibrium along our grounded ice boundary is mixed, with good agreement displayed for points along the Ross Ice Shelf edge and very poor agreement along the edge of the Amery Ice Shelf. We conclude from this that conversion of surface elevations to

ice thickness landward of the hydrostatic line should only be trusted if there is additional supporting data. The theoretical relationship between ice shelf thickness and the separation between the grounded ice boundary and the hydrostatic line is only weakly supported by our results. The major limitation is likely the positional uncertainty of the H points used to define the hydrostatic line, but these points did exhibit a broad spatial coherence less than the published two-kilometer uncertainty (Brunt et al., 2010b).

Undertaking this project was facilitated by the existence of the IPY and the primary objectives of this project were strongly influenced by the IPY objectives. This created benefits and disadvantages. The comprehensive nature of the product and the ability to divide the work among many participants were significant characteristics of ASAIID, but the need to create customized software that could run on multiple platforms as well as the need to carefully review and, in many cases, revise submissions from multiple participants were burdensome. Eventually, the ownership of this product by a large international team is a significant characteristic that will help establish these products as standards in the glaciological community. In addition, the documentation of the methodology should facilitate future efforts at monitoring both the grounded ice boundary and hydrostatic line. The software and products now available are allowing for the creation of educational activities that promise to increase the impact of ASAIID on future scientists.

Acknowledgements. A project of this magnitude and complexity could not have been accomplished without extensive contributions from many people, some of whom do not appear as authors on this paper. Funding support for the central work was provided through NASA grant 509496.02.08.01.81. Other domestic and international participants have been supported by other funding and we thank the British Antarctic Survey for adding flights specifically for ASAIID to an already packed field schedule. Michiel van den Broeke was extremely gracious for providing his work on firn correction values. Two anonymous reviewers contributed persuasive criticisms of an earlier draft that led to the extensive use of BEDMAP-compiled data and greatly improved the quantitative assessment of the ASAIID products' accuracies.

Edited by: I. M. Howat

References

- Alley, R. B., Blankenship, D. D., Rooney, S. T., and Bentley, C. R.: Sedimentation beneath ice shelves – the view from ice stream B, *Mar. Geol.*, 85, 101–120, 1989.
- Anandkrishnan, S., Voigt, D. E., Alley, R. R., and King, M. A.: Ice stream D flow speed is strongly modulated by the tide beneath the Ross Ice Shelf, *Geophys. Res. Lett.*, 30(7), 1361, doi:10.1029/2002GL016329, 2003.
- Bamber, J. L., Gomez-Dans, J. L., and Griggs, J. A.: A new 1 km digital elevation model of the Antarctic derived from combined satellite radar and laser data – Part 1: Data and methods, *The Cryosphere*, 3, 101–111, doi:10.5194/tc-3-101-2009, 2009.
- Bindschadler, R. A. and Vornberger, P. L.: Detailed elevation map of ice stream C using satellite imagery and airborne radar, *Ann. Glaciol.*, 20, 327–335, 1994.
- Bindschadler, R. A., Vornberger, P. L., King, M., and Padman, L.: Tidally-Driven Stick-Slip Motion in the Mouth of Whillans Ice Stream, Antarctica, *Ann. Glaciol.*, 36, 263–272, 2003.
- Bindschadler, R., Vornberger, P., Fleming, A., Fox, A., Mullins, J., Binnie, D., Paulsen, S. J., Granneman, B., and Gorodetzky, D.: The Landsat Image Mosaic of Antarctica, *Remote Sens. Environ.*, 112(12), 4214–4226, doi:10.1016/j.rse.2008.07.006, 2008.
- Bindschadler, R. A., Wichlacz, A., and Choi, H.: An Illustrated Guide to Using ASAIID Software, NASA Technical Memorandum, TM-2011-215879, 21 pp., 2011.
- Bohlander, J. and Scambos, T.: Antarctic coastlines and grounding line derived from MODIS Mosaic of Antarctica (MOA), Boulder, Colorado USA: National Snow and Ice Data Center, Digital media, 2007.
- Brunt, K. M., Fricker, H. A., Padman, L., and O'Neel, S.: ICESat-Derived Grounding Zone for Antarctic Ice Shelves, Boulder, Colorado USA: National Snow and Ice Data Center, Digital media, 2010a.
- Brunt, K. M., Fricker, H. A., Padman, L., Scambos, T. A., and O'Neel, S.: Mapping the grounding zone of the Ross Ice Shelf, Antarctica, Using ICESat laser altimetry, *Ann. Glaciol.*, 51(55), 71–79, 2010b.
- Corr, H. F. J., Doake, C. S. M., Jenkins, A., and Vaughan, D. G.: Investigations of an “ice plain” in the mouth of Pine Island Glacier, Antarctica, *J. Glaciol.*, 47(156), 51–57, 2001.
- Ferrigno, J. G., Mullins, J. L., Stapleton, J. A., Chavez, P. S., Velasco, M. G., Williams, R. S., Delinski, G. F., and Lear, D.: Satellite Image Map of Antarctica, U.S. Geological Survey, Miscellaneous Investigations Map Series, Map 1-2560, 1996.
- Fricker, H. A. and Padman, L.: Ice shelf grounding zone structure from ICESat laser altimetry, *Geophys. Res. Lett.*, 33, L15502, doi:10.1029/2006GL026907, 2006.
- Fricker, H. A., Coleman, R., Padman, L., Scambos, T. A., Bohlander, J., and Brunt, K. M.: Mapping the grounding zone of the Amery Ice Shelf, East Antarctica using InSAR, MODIS and ICESat, *Antarct. Sci.*, 21(5), 515–532, doi:10.1017/S095410200999023X, 2009.
- Joughin, I., Smith, B. E., and Holland, D. M.: Sensitivity of 21st Century Sea Level to Ocean-Induced Thinning of Pine Island Glacier, Antarctica, *Geophys. Res. Lett.*, 37, L20502, doi:10.1029/2010GL044819, 2010.
- Korona J., Berthier, E., Bernard, M., Remy, F., and Thouvenot, E.: SPIRIT. SPOT 5 stereoscopic survey of Polar Ice: Reference Images and Topographies during the fourth International Polar Year (2007–2009), *ISPRS J. Photogramm.*, 64, 204–212, 2009.
- Lee, D. S., Storey, J. C., Choate, M. J., and Hayes, R. W.: Four Years of Landsat-7 On-Orbit Geometric Calibration and Performance, *IEEE T. Geosci. Remote.*, 42(12), 2786–2795, doi:10.1109/TGRS.2004.836769, 2004.
- Liu, H., Jezek, K., Li, B., and Zhao, Z.: Radarsat Antarctic Mapping Project digital elevation model version 2, Boulder, CO: National Snow and Ice Data Center, Digital media, 2001.
- Lythe, M. B., Vaughan, D. G., and BEDMAP Consortium, BEDMAP: A new ice thickness and subglacial topographic model of Antarctica, *J. Geophys. Res.*, 106(B6), 11335–11351, 2001.

- Payne, A. J., Vieli, A., Shepherd, A. P., Wingham, D. J., and Rignot, E.: Recent dramatic thinning of largest West Antarctic ice stream triggered by oceans, *Geophys. Res. Lett.*, 31(23), L23401, doi:10.1029/2004GL021284, 2004.
- Payne, A. J., Holland, P. R., Shepherd, A. P., Rutt, I. C., Jenkins, A., and Joughin, I.: Numerical modeling of ocean-ice interactions under Pine Island Bay's ice shelf, *J. Geophys. Res.*, 112, C10019, doi:10.1029/2006JC003733, 2007.
- Pritchard, H. D., Arthern, R. J., Vaughan, D. G., and Edwards, L. A.: Extensive dynamic thinning on the margins of the Greenland and Antarctic ice sheets, *Nature*, 461, 971–975, doi:10.1038/nature08471, 2009.
- Rignot, E.: Tidal motion, ice velocity and melt rate of Petermann Gletscher, Greenland, measured from radar interferometry, *J. Glaciol.*, 42(142), 476–485, 1996.
- Rignot, E., Bamber, J. L., van den Broeke, M. R., Davis, C., Yonghong, L., van deBerg, W. J., and van Meijgaard, E.: Recent Antarctic ice mass loss from radar interferometry and regional climate modeling, *Nat. Geosci.*, 1, 106–110, doi:10.1038/ngeo102, 2008.
- Rignot, E., Mouginot, J., and Scheuchl, B.: Antarctic grounding line mapping from differential satellite radar interferometry, *Geophys. Res. Lett.*, 38, L10504, doi:10.1029/2011GL047109, 2011.
- Schoof, C.: Ice sheet grounding line dynamics: Steady states, stability, and hysteresis, *J. Geophys. Res.*, 112, F03S28, doi:10.1029/2006JF000664, 2007.
- Shepherd, A., Wingham, D. J., and Mansley, J. A. D.: Inland thinning of the Amundsen Sea sector, *Geophys. Res. Lett.*, 29(10), 1364, doi:10.1029/2001GL014183, 2002.
- Thomas, R., Rignot, E., Casassa, G., Kanagaratnam, P., Acuna, C., Akins, T., Brecher, H., Frederick, E., Gogineni, P., Krabill, W., Manizade, S., Ramamoorthy, H., Rivera, A., Russell, R., Sonntag, J., Swift, R., Yungel, J., and Zwally, J.: Accelerated sea-level rise from West Antarctica, *Science*, 306(5694), 255–258, 2004.
- Thomas, R. H., Stephenson, S. N., Bindschadler, R. A., Shabtaie, S., and Bentley, C. R.: Thinning and grounding line retreat on the Ross Ice Shelf, *Ann. Glaciol.*, 11, 165–172, 1988.
- van den Broeke, M. R., van de Berg, W. J., and van Meijgaard, E.: Firn depth correction along the Antarctic grounding line, *Antarct. Sci.*, 20(5), 1–5, doi:10.1017/S095410200800148X, 2008.
- Vaughan, D. G.: Tidal Flexure at Ice Sheet Margins, *J. Geophys. Res.*, 100(B4), 6213–6224, 1995.
- Wiens, D. A., Anandakrishnan, S., Winberry, J. P., and King, M. A.: Simultaneous teleseismic and geodetic observations of the stick-slip motion of an Antarctic ice stream, *Nature*, 453, 770–774, doi:10.1038/nature06990, 2008.
- Willey, R. L.: Generalized photogrammetry for Mariner 9, *Icarus*, 25, 613–626, 1975.
- Yamanokuchi, T., Doi, K., and Shibuya, K.: Validation of grounding line of the East Antarctic Ice Sheet derived by ERS-1/2 interferometric SAR data, *Polar Geoscience*, 18, 1–14, 2005.
- Zwally, H. J., Schutz, R., Bentley, C., Bufton, J., Herring, T., Minster, J., Spinhirne, J., and Thomas, R.: GLAS/ICESat L2 Antarctic and Greenland Ice Sheet Altimetry Data V001, Boulder, CO: National Snow and Ice Data Center, Digital media, 2003.